

This is a copy of the published version, or version of record, available on the publisher's website. This version does not track changes, errata, or withdrawals on the publisher's site.

Successive ferroelectric transitions induced by complex spin structures in Mn Bi₂S₄

Pavitra N. Shanbhag, Fabio Orlandi, Pascal Manuel, Martin Etter, Shrikant Bhat, and A. Sundaresan

Citation: Successive ferroelectric transitions induced by complex spin structures in MnBi₂S₄, Pavitra N. Shanbhag, Fabio Orlandi, Pascal Manuel, Martin Etter, Shrikant Bhat, and A. Sundaresan, Phys. Rev. B 109,

DOI: <https://doi.org/10.1103/PhysRevB.109.024401>


This version is made available in accordance with publisher policies. Please cite only the published version using the reference above. This is the citation assigned by the publisher at the time of issuing the APV. Please check the publisher's website for any updates.

Successive ferroelectric transitions induced by complex spin structures in MnBi_2S_4

Pavitra N. Shanbhag¹, Fabio Orlandi², Pascal Manuel², Martin Etter³, Shrikant Bhat³, and A. Sundaresan^{1,*}
¹*School of Advanced Materials, and Chemistry and Physics of Materials Unit, Jawaharlal Nehru Center for Advanced Scientific Research, Jakkur, Bangalore 560064, India*

²*ISIS Facility, Rutherford Appleton Laboratory, Chilton, Didcot OX11 0QX, United Kingdom*

³*Deutsches Elektronen-Synchrotron (DESY), Hamburg 22607, Germany*

 (Received 22 June 2023; revised 17 October 2023; accepted 20 November 2023; published 2 January 2024)

Our study reveals the emergence of ferroelectricity induced by incommensurate spin orders in the magnetic sulfide MnBi_2S_4 , which has a HgBi_2S_4 -type centrosymmetric monoclinic structure ($C2/m$). This compound reveals multiple magnetic transitions at $T_{N1} = 27$ K, $T_{N2} = 23$ K, and $T_{N3} = 21.5$ K, associated with three distinct incommensurate spin structures (ICM1, ICM2, and ICM3). ICM1 is described as an antiferromagnetic spin density wave with an incommensurate modulation vector $\mathbf{k}_1 = (0, \beta, \frac{1}{2})$ and magnetic superspace group $C\bar{1}.1'(\alpha, \beta, \gamma)0s$. While ICM2 has a similar propagation vector as ICM1, pyrocurrent measurements suggest the polar nature of this phase. This is further confirmed by neutron diffraction, which indicates a cycloidal structure with a magnetic superspace group $Bm.1'(0, \frac{1}{2}, \gamma)0s$. The magnetic ground state (ICM3) is a polar helical spin structure with magnetic space group $B2.1'(0, 0, \gamma)ss$ which is incommensurately modulated with propagation vector $\mathbf{k}_2 = (0, 0, \gamma)$ where $\gamma = 0.3793(1)$ (at 1.5 K).

DOI: [10.1103/PhysRevB.109.024401](https://doi.org/10.1103/PhysRevB.109.024401)

I. INTRODUCTION

In the past few decades, magnetoelectric multiferroics have garnered significant attention due to their unique ability to exhibit both ferroelectricity and magnetism, two properties that are typically mutually exclusive in classical ferroelectrics [1,2]. Consequently, it is challenging to obtain both ferroic properties in a single material [3], making single-phase magnetoelectric multiferroics extremely rare and highly sought after for their potential applications in spintronic and other devices [4,5]. Recently, spin-driven multiferroics have attracted considerable interest in condensed matter physics, as they exhibit ferroelectricity induced by specific magnetic structures that break spatial inversion symmetry at the magnetic ordering temperature in nonpolar compounds. These systems demonstrate strong coupling between magnetic and electrical order parameters due to the common origin of magnetism and ferroelectricity [1,6,7]. This discovery has led to extensive research into new multiferroic systems with different types of magnetism [6]. Researchers have proposed various mechanisms, such as the inverse Dzyaloshinskii-Moriya (DM) (or spin-current) model [8,9] and spin dependent $p-d$ orbital hybridization [10], to understand the magnetic origin of ferroelectricity. Materials such as TbMnO_3 [7], RMn_2O_5 [11], $\text{Ni}_3\text{V}_2\text{O}_8$ [12], MnWO_4 [13], $\text{Gd}_2\text{BaCuO}_5$ [14], and delafossites CuFeO_2 [15] and ACrO_2 ($A = \text{Ag, Cu}$) [16] are known to exhibit spin-driven multiferroicity. Often these materials present competing magnetic interactions leading to moderate magnetic frustration that give rise to noncollinear magnetic configurations such as cycloidal or proper screw helical spin structures [17–20]. The inverse DM model could successfully explain the spin induced multiferroicity due to the cycloidal

spin configuration in TbMnO_3 [7] and AgFeO_2 [21] but failed to account for proper screw helical spin configuration. Later, the extended inverse DM model developed by Kaplan and Mahanti provided local symmetry theory [22] that explained the microscopic origin for the spontaneous polarization induced by proper screw helical spin structure in some delafossites [23].

Recently, the exploration of multiferroic materials has expanded to include layered chalcogenides ACrS_2 ($A = \text{Ag, Cu}$), which are the sulfide analogs of the oxide delafossite family. AgCrS_2 crystallizes in a delafossite structure with the polar space group $R3m$. The structure consists of edge-sharing CrS_6 octahedra stacked in layers connected through AgS_4 tetrahedra along the c axis [24]. It undergoes a first-order phase transition at $T_N \sim 41.6$ K from paramagnetic rhombohedral structure ($R3m$) to antiferromagnetic monoclinic structure (Cm) [24,25]. Unlike spin-driven ferroelectric AgCrO_2 , AgCrS_2 belongs to geometric ferroelectric, in which ferroelectric polarization becomes measurable below T_N , arising from structural distortion induced by magnetic ordering [24]. Some Cr-based sulpho-spinels, such as ACr_2S_4 ($A = \text{Mn, Fe}$), show ferroelectricity [26,27], whereas $\text{A'Cr}_2\text{S}_4$ ($A' = \text{Cd, Hg}$) show relaxor behavior [28,29] coexisting with magnetic ordering. Notably, MnCr_2S_4 was reported to exhibit multiferroicity in two different temperature regions. It undergoes a first ferroelectric phase transition at the ferromagnetic transition temperature $T_C = 65$ K, and a second one at Yafet-Kittel (YK) magnetic phase transition temperature, $T_{YK} = 5$ K. It is reported that the ferroelectricity in the YK phase is spin driven and attributed to the inverse Dzyaloshinskii-Moriya interaction [26].

Recent investigation on another family of ternary manganese chalcogenide, MnSb_2X_4 ($X = \text{S, Se}$) crystallizing in the centrosymmetric monoclinic HgBi_2S_4 type structure with space group $C2/m$, reported to exhibit spin-driven ferro-

*Corresponding author: sundaresan@jncasr.ac.in

electricity [30,31]. Other members of the ternary manganese chalcogenide MnB_2X_4 ($B = \text{Sb, Bi}$; $X = \text{Se, Te}$) [32,33] reported to present interesting topological properties and are promising for understanding exotic topological quantum phenomena. In this view, we explored another member of the ternary manganese chalcogenide family, MnBi_2S_4 , known as mineral grafcianite [34]. Interestingly, we observe three successive magnetic phase transitions, two of which are associated with ferroelectricity. The different magnetic structures determined from high-resolution neutron diffraction study are a spin density wave, cycloidal, and helical spin structures where the latter two induce ferroelectricity.

II. EXPERIMENT

MnBi_2S_4 was synthesized by solid state reaction using a stoichiometric mixture of elemental Mn, Bi, and S powder in an evacuated silica tube by heating at 400 °C at the rate of 0.5 °C/min for 2 days. The heated powder was pressed into pellets and sintered at 700 °C for 8–10 days. Room-temperature synchrotron x-ray diffraction data were collected at the high-resolution synchrotron x-ray powder diffraction beamline P02.1 at the storage ring PETRA III (DESY, Hamburg, Germany) using the wavelength $\lambda = 0.20735$ Å with a Varex XRD4343CT detector at a sample to a detector distance of ~ 1000 mm [35]. Time-of-flight neutron powder diffraction (NPD) data were collected on the WISH instrument at the ISIS neutron and muon facility, UK [36]. Crystal and magnetic structure analysis was carried out by the Rietveld refinement method [37] using JANA2006 [38] and ISODISTORT software [39]. dc magnetization measurements were carried out with a magnetic property measurement system superconducting quantum interference device magnetometer (Quantum Design, USA), and heat capacity was measured in a physical property measurement system (PPMS). For the electrical measurements, both sides of the thin sintered sample pellet of 0.4 mm thickness were applied with silver paste covering an area of 12 mm². The temperature dependent dielectric constant at various magnetic fields was measured with an LCR meter (E4980A) with a warming rate of 2 K/min. Temperature dependent pyroelectric current was recorded with a Keithley 6517A electrometer at various magnetic fields. The sample was poled from 35 to 10 K under an applied electric field E , while cooling at the rate of 5 K/min. Then the sample was shorted for 20 min to remove the stray charges. Later, the pyrocurrent was recorded while warming at the rate of 10 K/min under zero and different magnetic fields. Temperature and magnetic field dependent dielectric and pyroelectric current measurements were carried out with the help of a multifunctional probe provided by Quantum Design using a PPMS. Electric polarization was determined by integrating pyroelectric current with time. For dc-biased current measurements, the sample was cooled to 10 K without any poling field. At 10 K, the dc electric field was applied, and the dc-biased current was recorded while warming with the rate of 10 K/min under the electric field.

III. RESULTS AND DISCUSSION

The monoclinic structure of MnBi_2S_4 with space group $C2/m$ has been confirmed through Rietveld refinement of

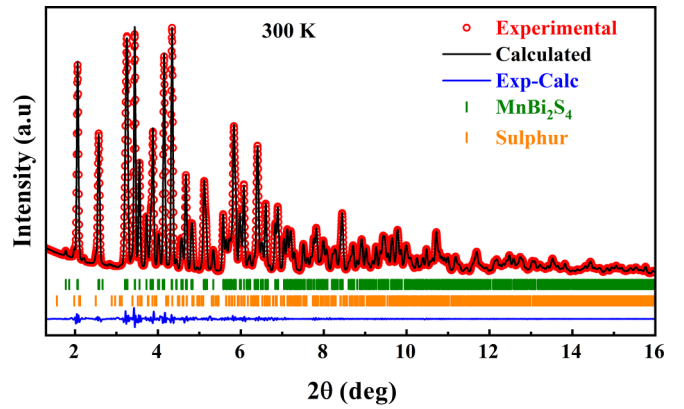


FIG. 1. Rietveld refined room-temperature synchrotron x-ray diffraction profile of MnBi_2S_4 at 300 K, using a wavelength of $\lambda = 0.20735$ Å. The reflections marked with the orange tick marks belong to an impurity phase of elemental sulfur with a weight fraction of 3.89(3)%. The tick marks represent the Bragg planes.

room-temperature synchrotron x-ray powder diffraction data. The refined profile of the synchrotron x-ray diffraction at room temperature is illustrated in Fig. 1, and the lattice parameters, atomic positions, and overall refinement factors are displayed in Table I. The crystal structure, as depicted in Fig. 2(a), consists of MnS_6 octahedra (pink) forming chains along the b axis with distorted BiS_5 polyhedra (blue) connected alternately to the MnS_6 octahedra in the ab plane. We observe a half-period shift of the Mn^{2+} atoms along the b axis between the chains, which can be termed as a zigzag configuration, as shown in Fig. 2(b). The nearest interchain and intrachain distances between Mn atoms for MnBi_2S_4 are indicated by dotted and solid pink lines in Fig. 2(b), respectively, and are compared with other known members of the ternary manganese chalcogenide family, MnB_2X_4 ($B = \text{Bi, Sb}$; $X = \text{S, Se}$) tabulated in Supplemental Material Table S1 [40]. The magnetic ordering of Mn atoms depends mainly on the interchain exchange coupling between the Mn atoms. The competition between intra- and interchain exchange coupling leads to magnetic frustration giving rise to the noncollinear magnetic ordering of Mn spins which is discussed later. In addition, we observe antisite cation disorder of Mn and Bi atoms, which might also contribute to magnetic frustration.

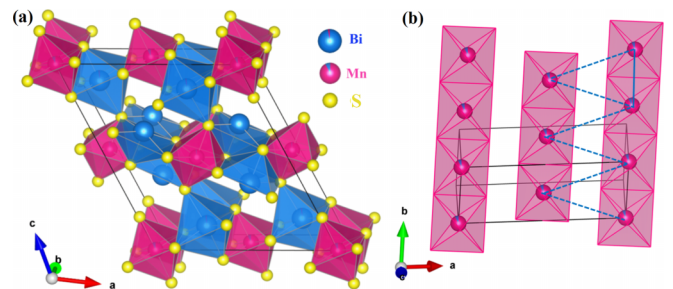


FIG. 2. (a) Crystal structure of MnBi_2S_4 in which edge-sharing MnS_6 octahedra forms chains along the b axis and are interconnected by bismuth sulphide polyhedra. (b) Nearest intrachain (solid line) and interchain (dotted line) distance between the Mn atoms in MnBi_2S_4 .

TABLE I. Rietveld refined structural parameters and R factors obtained from synchrotron XRD for MnBi_2S_4 at 300 K. Space group $C2/m$ (monoclinic); $a = 12.7535(6)$ Å, $b = 3.9109(1)$ Å, $c = 14.8491(7)$ Å, and $\alpha = \gamma = 90^\circ$, $\beta = 115.901(2)^\circ$; overall GoF = 5.2, $R_p = 2.32\%$, and $R_{wp} = 3.74\%$.

Atomic co-ordinates	x	y	z	U_{iso} (Å ²)	Occupancy
Mn1/Bi1' ($2a$)	0.0	0.0	0.0	0.0206(15)	0.924(2)/0.076(2)
Mn2/Bi2' ($2d$)	0.0	0.5	0.5	0.0196(16)	0.976(2)/0.024(2)
Bi1/Mn1' ($4i$)	0.3523(1)	0.0	0.1310(1)	0.0185(5)	0.977(3)/0.023(3)
Bi2/Mn2' ($4i$)	0.2854(1)	0.0	0.6389(1)	0.0182(5)	0.997(2)/0.003(4)
S2 ($4i$)	0.3406(6)	0.0	0.3268(6)	0.0323(2)	1.0
S1 ($4i$)	0.6577(5)	0.0	0.0518(4)	0.0039(25)	1.0
S3 ($4i$)	0.0098(6)	0.0	0.1766(5)	0.0214(21)	1.0
S4 ($4i$)	0.1146(6)	0.0	0.4590(5)	0.0169(20)	1.0

Figure 3(a) shows the temperature dependence of zero-field cooled (ZFC) and field cooled (FC) magnetization at different magnetic fields. We observe a broad magnetic anomaly near $T \sim 24$ K in the magnetization curve. Linear fit of inverse molar susceptibility versus temperature data as shown in Supplemental Material Fig. S1 [40], estimates the μ_{eff} value as $5.984(1)\mu_B$, which is close to the theoretical value of the Mn^{2+} spin-only moment, i.e., $5.92\mu_B$. The obtained value of paramagnetic Curie temperature (θ_{CW}) is

$-44.7(1)$ K, and the calculated frustration parameter $f = |\frac{\theta_{\text{CW}}}{T_N}| \approx 1.88$ indicates that magnetism is slightly frustrated [41]. The negative value of Curie-Weiss temperature and the nature of the $M(H)$ curve measured at 2 K [shown in the inset of Fig. 3(a)] suggest an antiferromagnetic ground state in MnBi_2S_4 .

Figure 3(b) presents the temperature dependence of specific heat divided by temperature, measured under 7 T and zero magnetic fields. The data indicates three lambda-type

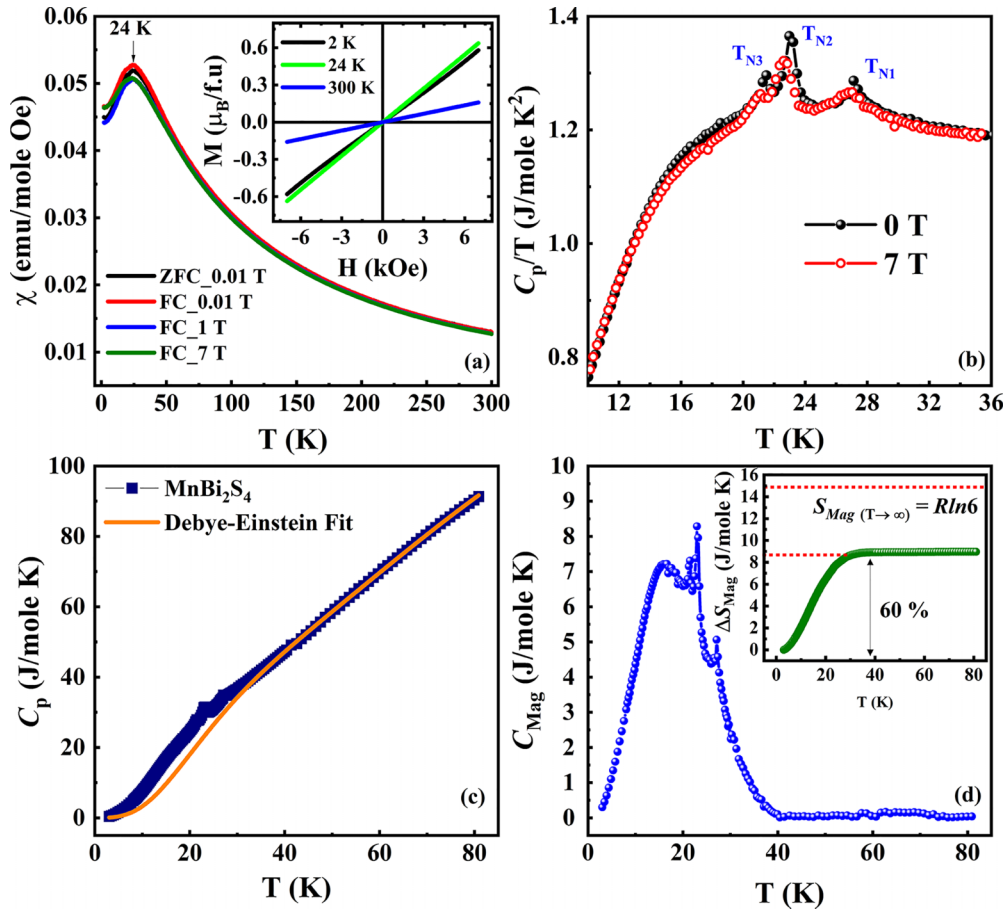


FIG. 3. (a) Temperature dependent dc magnetization measured under ZFC and FC conditions for various magnetic fields. The inset shows $M(H)$ curves measured at different temperatures. (b) Temperature dependent specific heat divided by temperature measured under zero and 7 T magnetic field. (c) Temperature dependent specific heat measured in zero magnetic field fitted with the Debye-Einstein model. (d) Magnetic contribution for specific heat as a function of temperature. Inset shows the change in magnetic entropy as a function of temperature.

anomalies in zero field, corresponding to three magnetic phase transitions at $T_{N1} = 27$ K, $T_{N2} = 23$ K, and $T_{N3} = 21.5$ K. In the presence of a 7 T magnetic field, the transition shifts slightly towards lower temperatures, and the peak becomes broader. To determine the change in magnetic entropy resulting from long-range antiferromagnetic ordering, the lattice contribution to the specific heat is obtained using the Debye-Einstein model [42], as discussed in the Supplemental Material [40]. Subsequently, the phonon contribution [Fig. 3(c)] is subtracted from the total specific heat to obtain the magnetic contribution of specific heat, as illustrated in Fig. 3(d). The expected change in entropy due to the magnetic ordering of Mn^{2+} ions with $S = 5/2$ is S_{mag} (at high T) = $R \ln(2S + 1) = 14.89$ J/mol K. The observed value of $\Delta S_{mag} = 8.96$ J/mol K [inset of Fig. 3(d)], which is almost 60% of the expected change in entropy.

The temperature dependencies of the real part of dielectric constant $\epsilon'(T)$ measured with 50 kHz at zero and different magnetic fields are shown in Fig. 4(a). A clear dielectric peak was observed at the magnetic ordering temperature T_{N2} in the absence of magnetic field. As the applied magnetic field increases, the dielectric peak slightly enhances, shifts to the lower temperature, and becomes broader, suggesting the occurrence of the magnetodielectric effect. A similar feature was observed in temperature dependent dielectric loss recorded at zero and various magnetic fields [Fig. 4(b)]. In addition to that, another dielectric anomaly was found at the magnetic ordering temperature T_{N3} and the magnified view is shown in the inset of Fig. 4(a). Due to the weak feature of this dielectric anomaly, no changes in the dielectric loss were observed at T_{N3} . Also, temperature dependent dielectric constant is measured at a warming rate of 1 K/min at various frequencies under zero magnetic field, as shown in Fig. 4(c). The dielectric anomalies observed at different frequencies appear at the same temperature (T_{N2}) without any shift, indicating that this anomaly has a magnetic origin. In addition, the dielectric dispersion observed below the transition temperature indicates the domain structure relaxation in $MnBi_2S_4$.

To investigate whether the observed dielectric anomalies are associated with ferroelectricity, temperature dependent pyroelectric current measurements were carried out with an applied electric field, $E = 6.25$ kV/cm, and different magnetic fields [see Fig. 5(a)]. In the absence of magnetic field, a sharp asymmetric pyrocurrent peak was observed at T_{N3} along with a small peak at T_{N2} . Upon increasing the applied magnetic field from 1 to 7 T, the intensity of the pyrocurrent peak at T_{N3} reduces, whereas that of T_{N2} enhances. Also, the pyrocurrent peaks shift towards low temperature with the application of magnetic field, consistent with the measured specific heat data. This is the total pyroelectric current, which accounts for the change of polarization with respect to temperature (primary contribution) and the change in polarization from thermal expansion combined with the piezoelectric effect (secondary contribution) in the material [43]. Polarization obtained by integrating the pyrocurrent trace with respect to time is shown in Fig. 5(b). Enhancement of the pyrocurrent peak at T_{N2} is clearly reflected in the polarization curve obtained at 7 T. The polarization value is $7 \mu\text{C}/\text{m}^2$ at 10 K under zero magnetic field, and no significant change was observed in the overall value of polarization at 10 K upon applying the

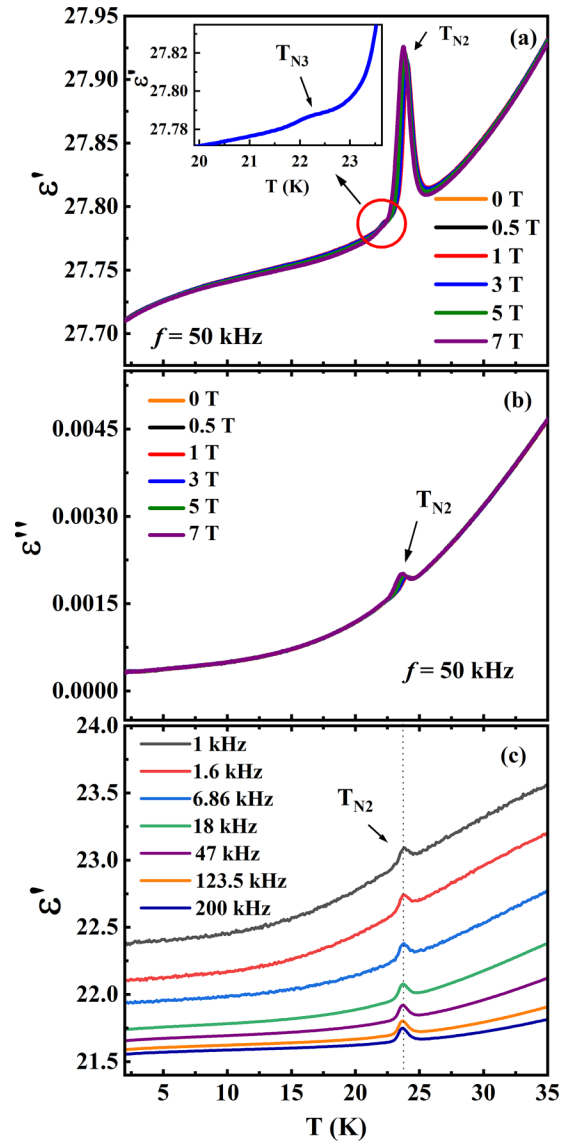


FIG. 4. (a) Temperature dependence of dielectric constant measured at 50 kHz under zero and various magnetic fields. Inset shows a zoomed-in image of the dielectric anomaly observed at T_{N3} . (b) Temperature dependence of dielectric loss measured under 50 kHz at zero and different magnetic fields. (c) Temperature dependence of dielectric constant measured at different frequencies under zero magnetic field.

magnetic field. Also, the switchability of the electric polarization was confirmed by reversing the poling electric field, as shown in Fig. 5(c). Further, to rule out the possible origin of the pyroelectric current peak due to thermally stimulated charge carriers and to confirm the occurrence of ferroelectric polarization at T_{N2} and T_{N3} , the dc-biased current was measured in the presence of an electric field while warming, without poling the sample [44,45]. We observe two pairs of consecutive polarization (positive) and depolarization (negative) peaks at T_{N2} and T_{N3} as depicted in Fig. 5(d). Thus, the appearance of ferroelectric polarization at magnetic ordering temperatures confirms magnetic order induced ferroelectricity in $MnBi_2S_4$.

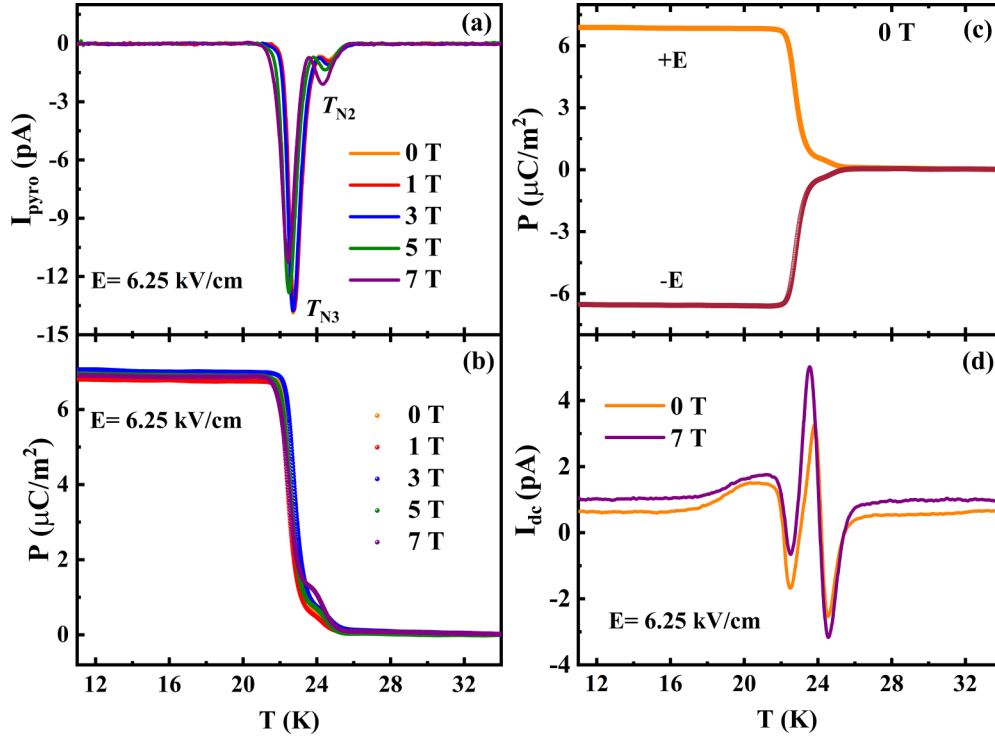


FIG. 5. Temperature dependence of (a) total pyroelectric current recorded for different magnetic fields with the poling electric field, E ; (b) the corresponding polarization; (c) switching of pyroelectric current by changing the direction of the poling electric field measured under zero magnetic field; and (d) dc-biased current measured in the presence of the electric field, E , under zero and 7 T magnetic field.

To understand the origin of ferroelectric polarization, we have carried out temperature dependent NPD measurements. A stack plot of time-of-flight NPD profiles collected at different temperatures in the range 40–1.5 K is shown in Fig. 6. NPD profiles from 40 to 28 K display reflections corresponding to the nuclear (paramagnetic) phase of MnBi_2S_4 , which can be indexed with monoclinic space group $C2/m$. At $T_{N1} = 27$ K, we can observe broad magnetic reflections due to short-range ordering, indicating the commencement of magnetic ordering of Mn^{2+} spins, as shown in Supplemental Material Fig. S2 [40]. Below 26 K, a new set of magnetic reflections (indicated with a black dotted line in Fig. 6) in the large d region appear. Using the `k_SEARCH` program in the `FULLPROF` suite [46], we have indexed these magnetic reflections using the incommensurate propagation vector $\mathbf{k}_1 = (0, \beta, \frac{1}{2})$ with $\beta \sim 0.3662(3)$ (at 26 K), and the associated incommensurate magnetic phase is termed as ICM1. Below ~ 22 K a set of new reflections (indicated with a red dotted line in Fig. 6) that can be indexed with the propagation vector $\mathbf{k}_2 = (0, 0, \gamma)$ with $\gamma \sim 0.37016(2)$ (at 22 K) appears at long d spacing. We observe the coexistence of both sets of magnetic reflections in the temperature range $22 < T < 17.5$ K. Here, the magnetic phase with propagation vector \mathbf{k}_1 becomes polar at $T \leq 22$ K and is termed as ICM2, which is discussed later in detail. For $17.5 \text{ K} < T < 1.5$ K, only the latter set of magnetic reflections is sustained, which can be indexed with $\mathbf{k}_2 = (0, 0, \gamma)$ alone, and this magnetic phase is termed as ICM3.

Firstly, the paramagnetic phase obtained at 40 K is in agreement with the $C2/m$ structural model. The Rietveld refinement profile and the related structural parameters at 40 K are shown in Fig. 7(a) and Supplemental Material Table

S2 [40], respectively. Further, knowing the crystal structure ($C2/m$) and propagation vector $\mathbf{k}_1 = (0, \beta, \frac{1}{2})$, we have investigated the possible magnetic modes and associated magnetic space groups for the ICM1 phase using the `ISODISTORT` package [39]. We found four possible magnetic structure models corresponding to two two-dimensional irreducible representations (irreps) with different order parameter directions. The correct magnetic superspace group is $C\bar{1}.1'(\alpha, \beta, \gamma)0s$ which can be obtained by superposition of two irreps, mU_1 with order parameter $(a, 0)$ and mU_2 with order parameter $(b, 0)$. The Rietveld refined NPD profile and the related structural parameters, along with the magnetic parameters at 24 K, are shown in Fig. 7(b) and Supplemental Material Table S3 [40], respectively. The obtained magnetic structure is incommensurately modulated with $\mathbf{k}_1 = (0, 0.3678(5), \frac{1}{2})$, an antiferromagnetic spin density wave (AFM SDW) propagating along the b axis with amplitude of $1.831(16)\mu_B$ and the Mn^{2+} moments oriented along the c direction, as shown in Fig. 8(a). Such AFM SDW was also observed in the multiferroic double perovskite compound NaNiWO_6 [47,48].

The observation of a spontaneous polarization below T_{N2} suggests a change in the magnetic structure since a SDW cannot break inversion symmetry. As explained above, two propagation vectors \mathbf{k}_1 and \mathbf{k}_2 are observed in the temperature region 22–17.5 K. Since the magnetic transition at T_{N2} and T_{N3} needs to be of the first order, due to the change of the propagation vector value, it is reasonable to assume that the ICM3 and ICM2 phases coexist in the $22 < T < 17.5$ K temperature range. Rietveld refined NPD data and the related structural and magnetic parameters at 21 K, are shown in Fig. 7(c) and Supplemental Material Tables S4(a) and S4(b)

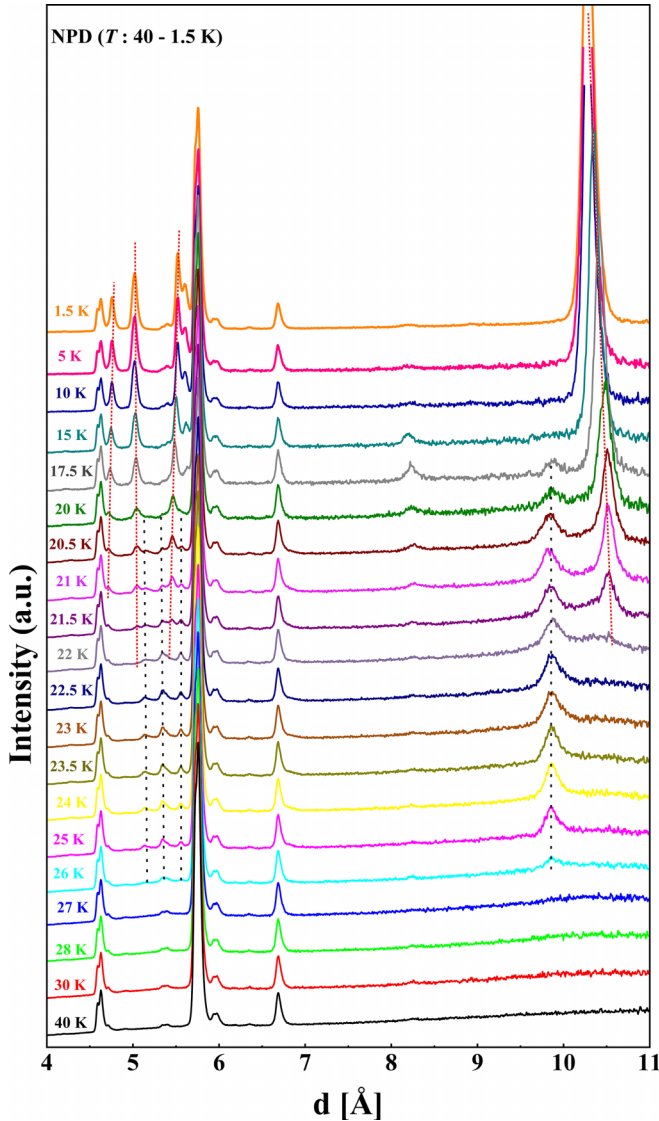


FIG. 6. Stack plot of time-of-flight NPD profiles collected using the WISH detector bank of average 2θ of 58.3° at different temperatures. The dotted black and red line acts as a guide to the eye representing magnetic reflections corresponding to the magnetic modulation vector \mathbf{k}_1 and \mathbf{k}_2 , respectively.

[40], respectively. The ICM2 spin structure corresponding to the propagation vector \mathbf{k}_1 is represented by the polar magnetic superspace group $Bm.1'(0, 1/2, \gamma)0s$ and is obtained by the superposition of two irreps mU_1 with order parameter $(a, 0)$ and mU_2 with order parameter $(b, 0)$. This structure consists of a cycloidal arrangement of the Mn^{2+} spins lying in the ac plane propagating along the c axis [shown in Fig. 8(b)] with a refined magnetic moment of $1.519(2)\mu_B$ at 21 K. Plotting the normalized intensity of the reflections corresponding to SDW/cycloid and helical phases with respect to temperature, as shown in Supplemental Material Fig. S3 [40], it is clear that the SDW peaks intensity drop slightly and then remain constant, which provides a hint of the SDW-cycloid transition below T_{N2} . This agrees with the temperature dependent heat capacity and polarization measurements, further suggesting a change from SDW to cycloid.

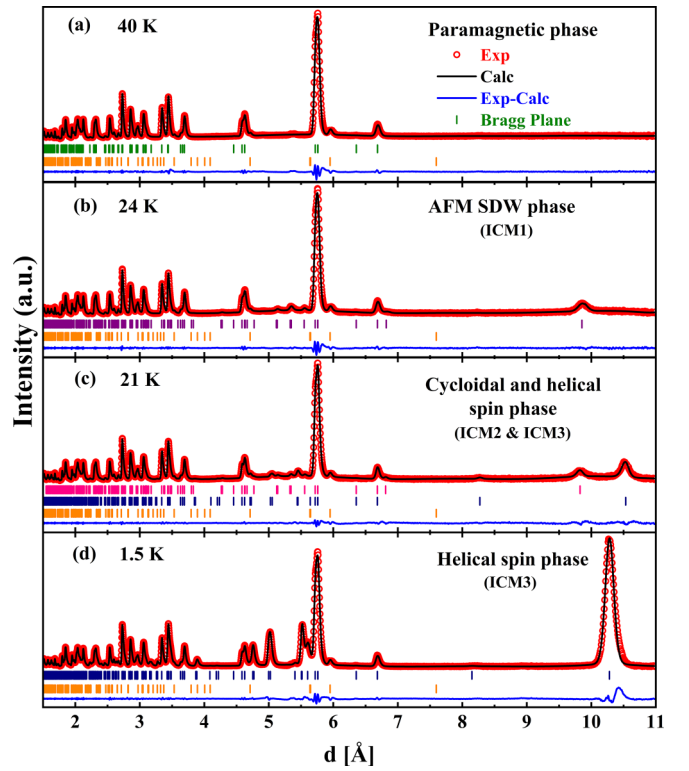


FIG. 7. Rietveld refined NPD profiles collected using the WISH detector bank of average 2θ of 58.3° at temperatures (a) 40 K, (b) 24 K, (c) 21 K, and (d) 1.5 K. The pink and blue tick marks in Fig. 7(c) correspond to cycloidal and helical magnetic phases, respectively. The reflections marked with the orange tick marks belong to an impurity phase of elemental sulfur with a weight fraction of 3.89(3)%. The tick marks represent the Bragg planes.

Finally, the magnetic ground state has been solved, using the details of crystal structure ($C2/m$) and propagation vector \mathbf{k}_2 . Symmetry analysis suggests four possible magnetic structure models corresponding to two two-dimensional irreps with different order parameter direction. The exact magnetic structure model is described by the polar magnetic space group $B2.1'(0, 0, \gamma)ss$, derived from the irrep $m\Lambda_2: (a, b)$. The obtained magnetic structure consists of a helical spin arrangement of Mn^{2+} moments propagating along the c axis [shown in Fig. 8(c)] with a refined magnetic moment of $4.083(14)\mu_B$ at 1.5 K and modulation vector $\mathbf{k}_2 = (0, 0, -0.3793(1))$. The adjacent magnetic moments along the c direction rotate at an angle $\alpha = 137^\circ$ (where $\alpha = 2\pi\mathbf{k}$) and an angle of 68.5° along the a axis. The Rietveld refined NPD profile and the related structural parameters, along with the magnetic parameters at 1.5 K, are shown in Fig. 7(d) and Supplemental Material Table S5 [40], respectively.

The magnetic structure investigation reveals that the crystal symmetry of AFM SDW retains the inversion center as indicated by the centrosymmetric magnetic point group, $\bar{1}1'$. This is consistent with the absence of polarization below T_{N1} and explains the paraelectric nature of MnBi_2S_4 . The ferroelectric polarization observed in MnBi_2S_4 in the ICM2 and ICM3 phases can be explained using the inverse DM model [49] or spin current model [9]. Usually, the exchange interaction between spins of transition metal ions is mediated

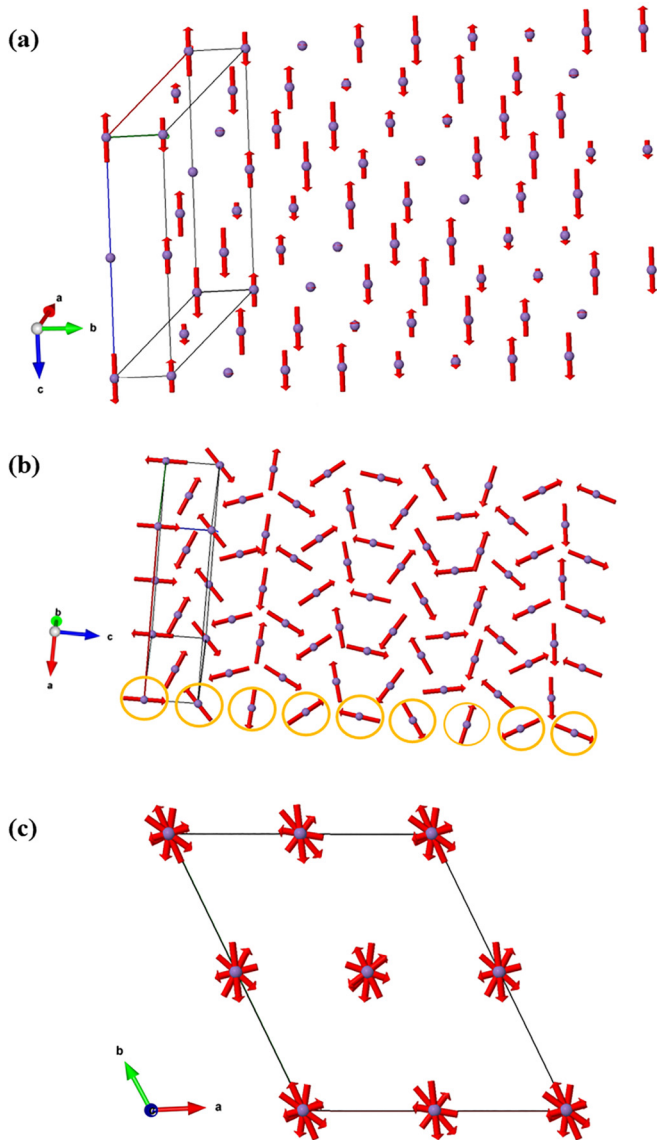


FIG. 8. (a) The Mn²⁺ spin arrangement in MnBi₂S₄ (at 24 K) with eight-unit cells showing AFM SDW propagating along the *b* axis. (b) The cycloidal Mn²⁺ spin configuration in MnBi₂S₄ (at 21 K) with eight-unit cells propagating along the *c* axis and spins lying in the *ac* plane in monoclinic cycloidal phase. (c) Helical arrangement of Mn²⁺ spins propagating along the *c* axis, where the adjacent spins are rotating at an angle of 137° in MnBi₂S₄.

by ligands, such as sulfur or oxygen ions. The DM interaction between the canted spins of cycloid, pushes negative ligand ions in the direction perpendicular to the spin chain formed by transition metal ions, resulting in spontaneous electric polarization perpendicular to the chain. Many oxides such as TbMnO₃, LiCuVO₄, Ni₃V₂O₈, LiCu₂O₂, MnWO₄, BaYFeO₄, Gd₂BaCuO₅, NaFeGe₂O₆, and CuO show ferroelectricity in their cycloidal spin structure [7,12,14,50–55] through an inverse DM mechanism. On the other hand, the helical configuration of Mn²⁺ spins rotating at an angle of 137° along the *c* direction can be considered as a proper screw spin type structure [30]. A similar spin arrangement is observed in MnSb₂S₄ in its ground state, which induces ferroelectric

polarization based on the inverse DM interaction model [30]. Let us understand the direction of ferroelectric polarization in the ICM2 and ICM3 phase based on the knowledge of magnetic point-group symmetry and a few theoretical models such as inverse DM and local symmetry theory for canted spin structures [9,21,49,55]. According to the inverse DM model, the polarization can be explained as $p_1 \alpha r_{ij} (S_i \times S_j)$. Hence, p_1 is expected to be perpendicular to both r_{ij} and $S_i \times S_j$, i.e., along the *a* axis of the parent *C2/m* structure in the cycloidal phase. Kaplan and Mahanti have reported that an additional term $p_2 \alpha (S_i \times S_j)$ also contributes to macroscopic polarization in both cycloidal and proper screw helical spin structures except in cases in which there is a mirror plane containing r_{ij} or a twofold rotation axis perpendicular to r_{ij} [22]. In MnBi₂S₄, the magnetic point group of cycloidal and helical spin structures is $m1'$ and $21'$, respectively. According to the symmetry, the mirror plane in the cycloidal magnetic phase contains r_{ij} , which results in the absence of a polarization component, p_2 . On the other hand, the twofold rotation axis in helical spin structure is along the direction of the propagation vector, so the plane of rotation of the spins in the helical phase is perpendicular to the twofold axis and as consequence r_{ij} is parallel to it. Hence, the polarization component, p_2 , is along the twofold axis in the helical phase, which is the direction of the *b* axis of the parent structure. Since the observation of multiferroicity in MnBi₂S₄ is purely of magnetic origin, the lone pair on bismuth does not contribute to the ferroelectric polarization. Hence, our studies clearly explain the absence of ferroelectricity below T_{N1} and the appearance of ferroelectric polarization below T_{N2} and T_{N3} using temperature dependent NPD experiments.

IV. CONCLUSIONS

We have demonstrated spin induced multiferroicity in centrosymmetric magnetic sulfide MnBi₂S₄. This compound exhibits three different magnetic phases, two of which were discovered to induce ferroelectricity. Using NPD, we have identified the magnetic structures ICM1, a centrosymmetric SDW; ICM2, a polar cycloidal structure; and finally, ICM3 as a polar helical structure. The emergence of ferroelectricity below T_{N2} and T_{N3} is explained using the inverse DM model between the noncollinear Mn²⁺ spins observed in the cycloidal and helical arrangement in MnBi₂S₄.

The raw data of the neutron diffraction experiment are available at [56].

ACKNOWLEDGMENTS

The authors would like to thank the Sheikh Saqr Laboratory and International Centre for Materials Science at Jawaharlal Nehru Centre for Advanced Scientific Research for providing experimental facilities. A.S. acknowledges DST, SERB, and the government of India for financial support. P.N.S. acknowledges Jawaharlal Nehru Centre for Advanced Scientific Research for support through a research fellowship (JNC/S0484). P.N.S. acknowledges Premakumar Yanda and Ravishankar P. N. for their help with electrical measurements and discussions related to magnetic structures. The authors acknowledge the Science and Technology Facility Council (STFC UK) for providing neutron beam time on the WISH

instrument (RB2000190). A.S. and P.N.S. acknowledge the P61B and P02.1 beamlines at PETRAIII, DESY Hamburg,

a member of the Helmholtz Association (HGF), for the synchrotron X-ray diffraction measurements.

- [1] D. Khomskii, Classifying multiferroics: Mechanisms and effects, *Physics* **2**, 20 (2009).
- [2] S.-W. Cheong and M. Mostovoy, Multiferroics: A magnetic twist for ferroelectricity, *Nat. Mater.* **6**, 13 (2007).
- [3] N. A. Hill, Why are there so few magnetic ferroelectrics?, *J. Phys. Chem. B* **104**, 6694 (2000).
- [4] R. Ramesh and N. A. Spaldin, Multiferroics: Progress and prospects in thin films, *Nat. Mater.* **6**, 21 (2007).
- [5] M. M. Vopson, Fundamentals of multiferroic materials and their possible applications, *Crit. Rev. Solid State Mater. Sci.* **40**, 223 (2015).
- [6] Y. Tokura, S. Seki, and N. Nagaosa, Multiferroics of spin origin, *Rep. Prog. Phys.* **77**, 076501 (2014).
- [7] T. Kimura, T. Goto, H. Shintani, K. Ishizaka, T. Arima, and Y. Tokura, Magnetic control of ferroelectric polarization, *Nature (London)* **426**, 55 (2003).
- [8] M. Mostovoy, Ferroelectricity in spiral magnets, *Phys. Rev. Lett.* **96**, 067601 (2006).
- [9] H. Katsura, N. Nagaosa, and A. V. Balatsky, Spin current and magnetoelectric effect in noncollinear magnets, *Phys. Rev. Lett.* **95**, 057205 (2005).
- [10] T.-h. Arima, Ferroelectricity induced by proper-screw type magnetic order, *J. Phys. Soc. Jpn.* **76**, 073702 (2007).
- [11] N. Hur, S. Park, P. A. Sharma, J. S. Ahn, S. Guha, and S. W. Cheong, Electric polarization reversal and memory in a multiferroic material induced by magnetic fields, *Nature (London)* **429**, 392 (2004).
- [12] G. Lawes, A. B. Harris, T. Kimura, N. Rogado, R. J. Cava, A. Aharony, O. Entin-Wohlman, T. Yildirim, M. Kenzelmann, C. Broholm, and A. P. Ramirez, Magnetically driven ferroelectric order in $\text{Ni}_3\text{V}_2\text{O}_8$, *Phys. Rev. Lett.* **95**, 087205 (2005).
- [13] K. Taniguchi, N. Abe, T. Takenobu, Y. Iwasa, and T. Arima, Ferroelectric polarization flop in a frustrated magnet MnWO_4 induced by a magnetic field, *Phys. Rev. Lett.* **97**, 097203 (2006).
- [14] P. Yanda, I. Golosovsky, I. Mirebeau, N. Ter-Oganessian, J. Rodríguez-Carvajal, and A. Sundaresan, Interplay of $4f$ - $3d$ interactions and spin-induced ferroelectricity in the green phase $\text{Gd}_2\text{BaCuO}_5$, *Phys. Rev. Res.* **2**, 023271 (2020).
- [15] T. Kimura, J. Lashley, and A. Ramirez, Inversion-symmetry breaking in the noncollinear magnetic phase of the triangular-lattice antiferromagnet CuFeO_2 , *Phys. Rev. B* **73**, 220401 (2006).
- [16] S. Seki, Y. Onose, and Y. Tokura, Spin-driven ferroelectricity in triangular lattice antiferromagnets ACrO_2 ($A = \text{Cu, Ag, Li, or Na}$), *Phys. Rev. Lett.* **101**, 067204 (2008).
- [17] A. Yoshimori, A new type of antiferromagnetic structure in the rutile type crystal, *J. Phys. Soc. Jpn.* **14**, 807 (1959).
- [18] O. Prokhnenko, R. Feyerherm, M. Mostovoy, N. Aliouane, E. Dudzik, A. U. B. Wolter, A. Maljuk, and D. N. Argyriou, Coupling of frustrated Ising spins to the magnetic cycloid in multiferroic TbMnO_3 , *Phys. Rev. Lett.* **99**, 177206 (2007).
- [19] J. K. Clark, C. Pak, H. Cao, and M. Shatruk, Helimagnetism in MnBi_2Se_4 driven by spin-frustrating interactions between antiferromagnetic chains, *Crystals* **11**, 242 (2021).
- [20] R. Shankar P N, F. Orlandi, P. Manuel, H.-J. Koo, M.-H. Whangbo, and A. Sundaresan, Factors governing the propagation direction and spin-rotation plane of noncollinear magnetic structures: A helix vs cycloid in doubly ordered perovskites NaYMnWO_6 and NaYNiWO_6 , *Inorg. Chem.* **60**, 15124 (2021).
- [21] N. Terada, D. D. Khalyavin, P. Manuel, Y. Tsujimoto, K. Knight, P. G. Radaelli, H. S. Suzuki, and H. Kitazawa, Spiral-spin-driven ferroelectricity in a multiferroic delafossite AgFeO_2 , *Phys. Rev. Lett.* **109**, 097203 (2012).
- [22] T. A. Kaplan and S. D. Mahanti, Canted-spin-caused electric dipoles: A local symmetry theory, *Phys. Rev. B* **83**, 174432 (2011).
- [23] N. Terada, Spin and orbital orderings behind multiferroicity in delafossite and related compounds, *J. Phys.: Condens. Matter* **26**, 453202 (2014).
- [24] F. Damay, C. Martin, V. Hardy, G. Andre, S. Petit, and A. Maignan, Magnetoelastic coupling and unconventional magnetic ordering in the multiferroic triangular lattice AgCrS_2 , *Phys. Rev. B* **83**, 184413 (2011).
- [25] F. Damay, S. Petit, M. Braendlein, S. Rols, J. Ollivier, C. Martin, and A. Maignan, Spin dynamics in the unconventional multiferroic AgCrS_2 , *Phys. Rev. B* **87**, 134413 (2013).
- [26] J. X. Wang, L. Lin, C. Zhang, H. F. Guo, and J.-M. Liu, Experimental observation of ferroelectricity in ferrimagnet MnCr_2S_4 , *Appl. Phys. Lett.* **117**, 032903 (2020).
- [27] L. Lin, H. X. Zhu, X. M. Jiang, K. F. Wang, S. Dong, Z. B. Yan, Z. R. Yang, J. G. Wan, and J.-M. Liu, Coupled ferroelectric polarization and magnetization in spinel FeCr_2S_4 , *Sci. Rep.* **4**, 1 (2014).
- [28] J. Hemberger, P. Lunkenheimer, R. Fichtl, H.-A. K. Von Nidda, V. Tsurkan, and A. Loidl, Relaxor ferroelectricity and colossal magnetocapacitive coupling in ferromagnetic CdCr_2S_4 , *Nature (London)* **434**, 364 (2005).
- [29] S. Weber, P. Lunkenheimer, R. Fichtl, J. Hemberger, V. Tsurkan, and A. Loidl, Colossal magnetocapacitance and colossal magnetoresistance in HgCr_2S_4 , *Phys. Rev. Lett.* **96**, 157202 (2006).
- [30] C. De, N. Ter-Oganessian, and A. Sundaresan, Spin-driven ferroelectricity and large magnetoelectric effect in monoclinic MnSb_2S_4 , *Phys. Rev. B* **98**, 174430 (2018).
- [31] J. Alonso, M. Martínez-Lope, M. Casais, and M. Fernández-Díaz, Evolution of the Jahn–Teller distortion of MnO_6 octahedra in RMnO_3 perovskites ($R = \text{Pr, Nd, Dy, Tb, Ho, Er, Y}$): A neutron diffraction study, *Inorg. Chem.* **39**, 917 (2000).
- [32] Y. Deng, Y. Yu, M. Z. Shi, Z. Guo, Z. Xu, J. Wang, X. H. Chen, and Y. Zhang, Quantum anomalous Hall effect in intrinsic magnetic topological insulator MnBi_2Te_4 , *Science* **367**, 895 (2020).
- [33] H. Zhang, W. Yang, Y. Wang, and X. Xu, Tunable topological states in layered magnetic materials of MnSb_2Te_4 , MnBi_2Se_4 , and MnSb_2Se_4 , *Phys. Rev. B* **103**, 094433 (2021).
- [34] C. L. Ciobanu, J. Brugger, N. J. Cook, S. J. Mills, P. Elliott, G. Damian, and F. Damian, Grațianite, MnBi_2S_4 , a new mineral

- from the Băița Bihor skarn, Romania, *Am. Mineral.* **99**, 1163 (2014).
- [35] A.-C. Dippel, H.-P. Liermann, J. T. Delitz, P. Walter, H. Schulte-Schrepping, O. H. Seeck, and H. Franz, Beamline P02.1 at PETRA III for high-resolution and high-energy powder diffraction, *J. Synchrotron Radiat.* **22**, 675 (2015).
- [36] L. C. Chapon, P. Manuel, P. G. Radaelli, C. Benson, L. Perrott, S. Ansell, N. J. Rhodes, D. Raspino, D. Duxbury, E. Spill, and J. Norris, Wish: The new powder and single crystal magnetic diffractometer on the second target station, *Neutron News* **22**, 22 (2011).
- [37] H. Rietveld, A profile refinement method for nuclear and magnetic structures, *J. Appl. Crystallogr.* **2**, 65 (1969).
- [38] V. Petříček, M. Dušek, and L. Palatinus, Crystallographic computing system JANA2006: General features, *Z. Kristallogr. – Cryst. Mater.* **229**, 345 (2014).
- [39] H. T. Stokes, D. M. Hatch, B. J. Campbell, and D. E. Tanner, ISODISPLACE: A web-based tool for exploring structural distortions, *J. Appl. Crystallogr.* **39**, 607 (2006).
- [40] See Supplemental Material at <http://link.aps.org/supplemental/10.1103/PhysRevB.109.024401> for the Debye-Einstein model with the obtained Debye and Einstein temperatures, the Curie Weiss fit in the paramagnetic region of inverse magnetic susceptibility data, the intensity difference plot obtained from the time-of-flight NPD profiles collected at 27 and 40 K showing diffuse scattering at TN1, the temperature dependence of the normalized intensity of magnetic satellites corresponding to the helical and cycloid/SDW magnetic phase, the tabulated intra- and interchain distances for different ternary manganese chalcogenide, and the tabulated Rietveld refined structural and magnetic moment parameters obtained from the time-of-flight NPD data collected at 40, 24, 21, and 1.5 K for MnBi₂S₄.
- [41] S. Lee, A. Pirogov, M. Kang, K. H. Jang, M. Yonemura, T. Kamiyama, S. W. Cheong, F. Gozzo, N. Shin, H. Kimura, and Y. Noda, Giant magneto-elastic coupling in multiferroic hexagonal manganites, *Nature (London)* **451**, 805 (2008).
- [42] S. Ghara, N. Ter-Oganessian, and A. Sundaresan, Linear magnetoelectric effect as a signature of long-range collinear antiferromagnetic ordering in the frustrated spinel CoAl₂O₄, *Phys. Rev. B* **95**, 094404 (2017).
- [43] T. Tong, J. Karthik, R. Mangalam, L. W. Martin, and D. G. Cahill, Reduction of the electrocaloric entropy change of ferroelectric PbZr_{1-x}Ti_xO₃ epitaxial layers due to an elastocaloric effect, *Phys. Rev. B* **90**, 094116 (2014).
- [44] C. De, S. Ghara, and A. Sundaresan, Effect of internal electric field on ferroelectric polarization in multiferroic TbMnO₃, *Solid State Commun.* **205**, 61 (2015).
- [45] N. Terada, Y. S. Glazkova, and A. A. Belik, Differentiation between ferroelectricity and thermally stimulated current in pyrocurrent measurements of multiferroic *M*Mn₇O₁₂ (*M* = Ca, Sr, Cd, Pb), *Phys. Rev. B* **93**, 155127 (2016).
- [46] J. Rodriguez-Carvajal, Diffraction using the program FullProf, in *Applied Crystallography* (World Scientific, Singapore, 2001), p. 30.
- [47] R. Shankar P N, F. Orlandi, P. Manuel, W. Zhang, P. S. Halasyamani, and A. Sundaresan, A-site and B-site cation ordering induces polar and multiferroic behavior in the perovskite NaLnNiWO₆ (*Ln* = Y, Dy, Ho, and Yb), *Chem. Mater.* **32**, 5641 (2020).
- [48] H.-J. Koo, R. Shankar P. N., F. Orlandi, A. Sundaresan, and M.-H. Whangbo, On ferro- and antiferro-spin-density waves describing the incommensurate magnetic structure of NaYNiWO₆, *Inorg. Chem.* **59**, 17856 (2020).
- [49] I. A. Sergienko and E. Dagotto, Role of the Dzyaloshinskii-Moriya interaction in multiferroic perovskites, *Phys. Rev. B* **73**, 094434 (2006).
- [50] Y. Naito, K. Sato, Y. Yasui, Y. Kobayashi, Y. Kobayashi, and M. Sato, Ferroelectric transition induced by the incommensurate magnetic ordering in LiCuVO₄, *J. Phys. Soc. Jpn.* **76**, 023708 (2007).
- [51] O. Heyer, N. Hollmann, I. Klassen, S. Jodlauk, L. Bohatý, P. Becker, J. Mydosh, T. Lorenz, and D. Khomskii, A new multiferroic material: MnWO₄, *J. Phys.: Condens. Matter* **18**, L471 (2006).
- [52] S. Park, Y. Choi, C. Zhang, and S.-W. Cheong, Ferroelectricity in an *S* = 1/2 chain cuprate, *Phys. Rev. Lett.* **98**, 057601 (2007).
- [53] J.-Z. Cong, S.-P. Shen, Y.-S. Chai, L.-Q. Yan, D.-S. Shang, S.-G. Wang, and Y. Sun, Spin-driven multiferroics in BaYFeO₄, *J. Appl. Phys.* **117**, 174102 (2015).
- [54] T. Kimura, Y. Sekio, H. Nakamura, T. Siegrist, and A. Ramirez, Cupric oxide as an induced-multiferroic with high-*T*_C, *Nat. Mater.* **7**, 291 (2008).
- [55] L. Ding, P. Manuel, D. D. Khalyavin, F. Orlandi, and A. A. Tsirlin, Unraveling the complex magnetic structure of multiferroic pyroxene NaFeGe₂O₆: A combined experimental and theoretical study, *Phys. Rev. B* **98**, 094416 (2018).
- [56] <https://doi.org/10.5286/ISIS.E.RB2000190>.